Quantitative imaging through a spectrograph. 2. Stoichiometry mapping by Raman scattering

René A. L. Tolboom, Nico J. Dam, and Hans ter Meulen

The Bayesian deconvolution algorithm described in a preceding paper [Appl. Opt. **43,** 5669–5681 (2004)] is applied to measurement of the two-dimensional stoichiometry field in a combustible methane–air mixture by Raman imaging through a spectrograph. Stoichiometry (fuel equivalence ratio) is derived from the number density fields of methane and nitrogen, with a signal-to-noise ratio of ~10 in a 600-laser-shot average. Prospects for single-shot Raman imaging are discussed. © 2004 Optical Society of America

OCIS codes: 100.1830, 280.1740, 290.5860.

1. Introduction

In a companion paper[1] (referred to hereafter as T1) the way in which a spectrograph mixes spatial and spectral information for a single light source of finite (nonzero) dimensions was described. Our main aim in that paper was to show that the spatial information can be extracted from the entangled data by use of a dedicated linear Bayesian deconvolution filter. In this paper we demonstrate this procedure on a particularly interesting example, viz., determination of a two-dimensional (2-D) stoichiometry map of a combustible (but nonburning) methane–air mixture by Raman imaging through a spectrograph. The technique described in this paper was also applied to the spectroscopically easier case of a dry-air flow.[2]

The stoichiometry of a fuel–oxidizer mixture is one of the key parameters that characterize a combustion process. It can be used to predict reaction pathways and the gross behavior of the mixture after ignition.[3,4] The practical measurement of the local stoichiometry tends to be complicated because the local mole fractions of at least two different chemical species (fuel and oxidizer; both may be one or several compounds) have to be determined simultaneously. Optical techniques are attractive candidates for accomplishing this because of their nonintrusive nature and their potentially good spatial and temporal resolution.[5,6] For quantitative purposes, Raman-scattering diagnostics has the advantage of a straightforward interpretation of the scattered-light intensities in terms of molecular number densities (no quenching correction is required, as it is for laser-induced fluorescence).[7] Because of its low signal strength, however, Raman scattering requires highly selective spectral filtering. A spectrograph is arguably the best choice for filtering, because it simultaneously provides a check on the spectral purity of the recorded data. Direct imaging through a spectrograph, however, produces a convolution of spectral and spatial information on the entrance slit and therefore requires use of a postprocessing step to deconvolve the two. This postprocessing step was the subject of companion paper T1.

In Section 2 of this paper we adapt the convolution–deconvolution algorithm for imaging through an optical multichannel analyzer (OMA; an imaging grating spectrograph equipped with a CCD camera on its exit port), as described in paper T1, to the case of multispecies Raman-scattered light. In Section 3 we describe the experimental setup, followed by a discussion of the Raman spectrum of the methane–air mixture. Subsequently we provide results on determination of the density field of the relevant chemical species and on the stoichiometry field derived from them. The paper concludes with a brief discussion of the prospects for single-shot OMA Raman imaging.

2. Two-Dimensional Multispecies Raman Imaging through a Spectrograph

The measurements discussed in this paper all concern quantitative density field determinations based on Raman scattering in gaseous media. For this

The authors are with the Applied Physics Group, Radboud University of Nijmegen, Toernooiveld 1, 6525 ED Nijmegen, The Netherlands. N. J. Dam's e-mail address is nicod@science.ru.nl.

Received 24 December 2003; revised manuscript received 16 July 2004; accepted 27 July 2004.

0003-6935/04/305682-09$15.00/0

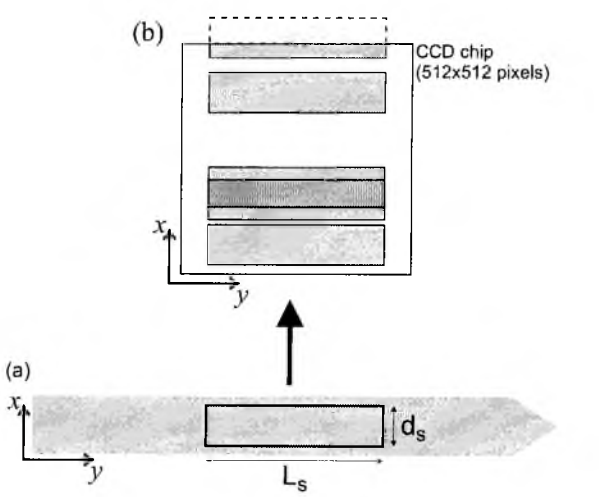

Fig. 1. Schematic experimental configuration. (a) A thin ribbon of light (light gray) illuminates a sample. The probe volume, enclosed by the black box rule, is imaged onto the entrance slit of an imaging spectrograph with fixed length L_s and adjustable width d_s. The line of sight is perpendicular to the plane of the figure. (b) Each wavelength component in the scattered light produces one subimage of the probe volume on the exit plane of the spectrograph, some of them on the CCD detector chip. (Here we indicate schematically the hypothetical case of five discrete wavelength components, two of which produce overlapping subimages.)

reason we extend the discussion of paper T1 to the specific case of OMA Raman imaging. In particular, the identification of the various quantities that appear in the convolution–deconvolution formalism of paper T1 will receive attention.

The specific experimental configuration that we discuss is schematically shown in Fig. 1(a). A thin sheet of light (light gray in the figure) illuminates a (gas phase) sample. Scattered light is imaged onto the entrance slit of a spectrograph (the field of view is enclosed by a black box rule) and detected by a CCD chip in its exit plane. The system is aligned such that the coordinate system that is adopted (x, y) is aligned with (pixel columns, pixel rows) of the CCD and with the (height, propagation direction) of the laser sheet, respectively. Spectral dispersion in the spectrograph takes place along the x direction, and we assume perfect imaging along the y direction.

Under monochromatic illumination, the spectrograph projects exactly one faithful image of the entrance slit onto the exit plane, on a location (along x) that depends on the wavelength of the incident light. Under polychromatic illumination, each wavelength component produces such an image [Fig. 1(b)], which may or may not overlap others, depending on the spectral structure of the input (and on the technical specifications and settings of the spectrograph, of course). It has been shown that the (spectrally integrated) intensity distribution in the spectrograph's exit plane takes the form of a one-dimensional convolution of the spectral and the spatial intensity distributions on the entrance slit (see paper T1); that is,

$$T(x, y) = S_\lambda(y, \lambda) * S(x_{\text{in}}, y), \tag{1}$$

in which T is the power incident upon pixel (x, y) in the exit plane and S_λ and S denote spectral and spatial intensity distributions, respectively, on the entrance slit. The asterisk denotes the convolution of both signals, which involves the x direction only. In companion paper T1 we described the Bayesian deconvolution procedure that reconstructs $S(x_{\text{in}}, y)$ from $T(x, y)$, given spectral structure S_λ, in the presence of noise in the recorded data [noise is neglected in Eq. (1)]. This formalism is tailored to the particular situation of Fig. 1 in Subsection 2.D below.

When several chemical species contribute different wavelength components to the Raman-scattered light, a main point of concern is the factorizability assumption of Eq. (4) of paper T1, that is, on whether the wavelength- and position-dependent scattered-light intensity distribution can be factored into components that, for each strip, depend only on wavelength or position:

$$S(x, y; \lambda) \stackrel{?}{=} S_\lambda(y; \lambda) S(x, y). \tag{2}$$

Note that the factorizability assumption involves only the coordinate in the plane of spectral diffraction. Individual strips can be treated separately [assuming sufficiently high-quality imaging optics, such that the point-spread function can be neglected], and we will suppress the y index in what follows. For the time being, the (x, y) coordinates are taken to label both pixels on the CCD and the corresponding probe volume element (voxel) in the illuminated sample. The thickness of the sheet of light (z direction, along the line of sight of the detection system) is assumed to be well within the depth of field of the imaging optics.

Even with monochromatic incident light, the Raman-scattered light in general contains several wavelength components, depending on the chemical composition of the scattering volume. As discussed in paper T1, the spectrograph will produce an individual image in the exit plane for every wavelength component. The factorizability assumption is justified if the spectrum is sufficiently sparse that the images that are due to individual wavelength components do not overlap, or if the images do overlap but all the components arise from the same spectral source. (These conditions are sufficient but not exclusive; other conditions in which the factorizability assumption is justified exist but are less general, and they are not considered here.)

The spectral power scattered by a small voxel in the field of view can be written as

$$P(\lambda, x) \propto \sum_{s,i} N_i^{(s)}(x) I_L(x) \sigma_i^{(s)}(\lambda) \tag{3}$$

for every strip y. In relation (3) the first two factors denote the population (number density) $N_i^{(s)}$ of a particular scatterer (molecule of a specific chemical species s in a specific quantum state i) and of the local laser intensity I_L, respectively. Both may depend on

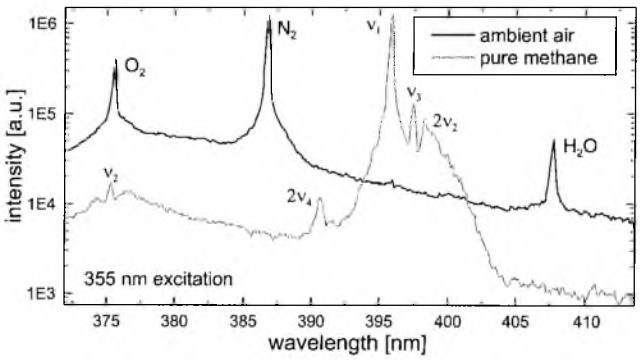

Fig. 2. Raman spectra of ambient air and of pure methane [1 bar (10^5 Pa)]. Note the logarithmic ordinate; the curves have been offset for clarity. The spectra were recorded through a spectrograph with a 1200-groove/mm grating using 355-nm light (tripled Nd:YAG laser) for illumination. The N_2 band and the strongest CH_4 (ν_1, ν_3, $2\nu_2$) bands are isolated, but the O_2 band overlaps a weak (ν_2) CH_4 band. There is also a relatively small contribution of water vapor in the ambient air spectrum.

position. The last factor of relation (3) is the total Raman-scattering cross section, which (for every chemical species and every initial quantum state) includes contributions from all possible final quantum states and contains all wavelength dependence. The summation extends over all chemical species and all initial quantum states, and it is because of this summation that relation (3) is not automatically separable.

In this paper we deal with the specific case of a combustible mixture of methane (CH_4) and air (N_2–O_2). The Raman spectra of Fig. 2 (main constituents listed in Table 1) show that O_2 and N_2 behave quite differently from CH_4. Whereas O_2 and N_2 each give rise to essentially just one scattered wavelength (Q branch[5]; their width is due to the finite resolving power of the spectrograph plus a small effect caused by nonzero rotational distortion), the Raman spectrum of CH_4 is much more complex, with contributions from various vibrational bands as well as rotational envelopes.

Two issues now require special attention, viz. (i) the overlap of the fundamental O_2 Raman band with one of the CH_4 lines (see Fig. 2 at $\lambda \approx 375$ nm) and (ii) the spectral structure of the main CH_4 Raman lines (at $\lambda \approx 395$–400 nm).

Table 1. Assignments,[a] Raman Shifts, and Peak Positions ($\lambda_{248/355}$) of the Raman Bands Observed in a Methane–Air Mixture on 248- and 355-nm Illumination

Compound	Assignment	Shift (cm^{-1})	λ_{248} (nm)	λ_{355} (nm)
O_2	ν_0	1556	258	376
N_2	ν_0	2331	263	387
CH_4	ν_2	1520	258	375
	$2\nu_4$	2580	265	391
	ν_1, ν_3, $2\nu_2$	2914	267–270	395–400
H_2O	ν_1	3635	273	408

[a]From Refs. 5, 8, and 9.

A. Overlap of O_2 and CH_4 Raman Lines

Stoichiometry Φ of a methane–air mixture is defined here as

$$\Phi(x, y) = \frac{[CH_4](x, y)/[O_2](x, y)}{([CH_4]/[O_2])|_{stoich}} = \frac{2[CH_4](x, y)}{[O_2](x, y)}, \quad (4)$$

in which the brackets indicate number densities. Thus Φ corresponds to the fuel equivalence ratio.[4] To determine Φ we must measure $[CH_4]$ and $[O_2]$ separately. From Fig. 2 it follows that CH_4 makes an unambiguous contribution to the Raman spectrum (broad band system centered at 397 nm) but O_2 does not: The ν_2 band of CH_4 cannot be spectrally separated from the fundamental O_2 band. As a result, the determination of $[O_2]$ on the basis of the Raman intensity at 375 nm becomes ambiguous, especially in fuel-rich regions.

There are two solutions to this problem. One is to correct the combined O_2–CH_4 Raman signal at 375 nm for the CH_4 contribution by using the CH_4 concentration that can be determined from the 397-nm band. The other solution is to exploit the fact that, in the nonburning mixture, the $[N_2]$:$[O_2]$ ratio is constant, say, β, so Φ can also be written as

$$\Phi(x, y) = \frac{2[CH_4](x, y)}{[O_2](x, y)} = \frac{2\beta[CH_4](x, y)}{[N_2](x, y)}. \quad (5)$$

The contribution of N_2 to the Raman spectrum is well separated (with 355-nm illumination) from that of the other components, so $[N_2]$ can be determined directly from the Raman intensity. We followed the second approach for the research described in this paper.

B. Temperature

There is one more caveat that needs to be discussed, and that is the temperature distribution over the field of view. Temperature affects the population distribution over available quantum states, and, inasmuch as different states possess different Raman-scattering cross sections and give rise to spectral lines at different Raman shifts, the shape of the rotational envelope of any Raman band will depend on temperature. For Q-branch Raman scattering, as in the cases of O_2 and N_2, this will be only a marginal effect (their widths are at the resolution limit of the equipment anyway), but for extended spectral structures like that of CH_4 it may preclude factorization of relation (3) (depending on the range of temperature variation, of course).

To estimate the influence of temperature on the spectral structure we made a (fairly crude) simulation of the methane Raman bands in the 400-nm range of Fig. 2 (ν_1, ν_3, and $2\nu_2$ at an $\sim$3000-cm^{-1} Raman shift). Band strengths were scaled to match the experimentally found relative intensities, and individual rotational line strengths were scaled with the appropriate statistical weights and a Boltzmann factor. We calculated rotational energy levels in the

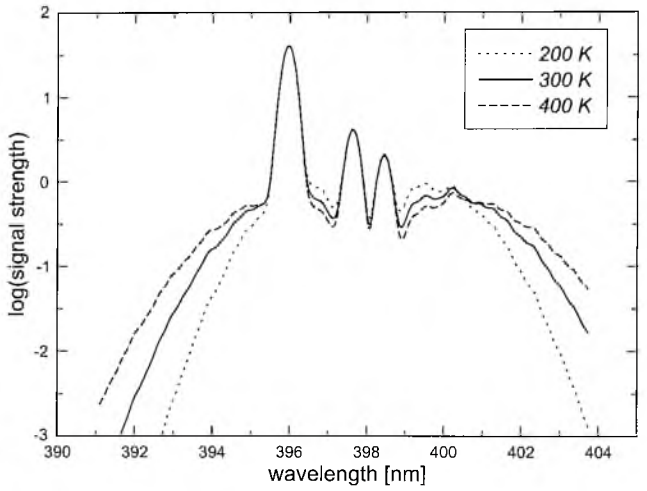

Fig. 3. Simulated methane Raman spectrum near a 3000-cm^{-1} Raman shift under 355-nm illumination. See text for details of the calculation. The three spectra correspond to three different temperatures. Note the logarithmic ordinate.

rigid spherical top approximation, neglecting the difference in B constants for various vibrational states. $B = 5.25\ cm^{-1}$ was taken throughout, and only the three strongest branches of the ν_3 band were taken into account.[8] A Gaussian instrumental linewidth of 10 cm^{-1} (0.16 nm) was assumed. Figure 3 shows the calculated band contours for temperatures ranging from 200 to 400 K. Evidently there are only minor differences in the spectral envelopes over this temperature range (note the logarithmic ordinate) because the strongest contributions to the spectrum all arise from Q branches. We conclude, therefore, that the assumption of constant temperature is hardly restrictive for vibrational OMA Raman-scattering experiments of flows near room temperature.

The factorization of Eq. (2) can thus be completed for all individual Raman bands, resulting in

$$S_\lambda(\lambda) = \sum_i \sigma_i(\lambda) \frac{g_i \exp[-(E_i/k_B T)]}{Z}, \qquad (6a)$$

$$S(x) = N(x) I_L(x) \Delta t, \qquad (6b)$$

in which Δt denotes the recording time (gate width), Z is the partition function, g_i is a degeneracy factor, k_B is Boltzmann's constant, and T is the absolute temperature. E_i is the energy of initial (rovibrational) quantum state i.

C. Spectral Width of the Main CH_4 Band

The strongest feature in the Raman spectrum of CH_4, ~397 nm, is in fact a complex structure that involves three Raman-active vibrational modes (Table 1). Effectively, therefore, this Raman band has a width of approximately 5 nm (with 355-nm incident light). When the entrance slit of the spectrograph is broadened, the spatial structure is entangled with this spectral profile according to the convolution integral of Eq. (8) of paper T1. For the calculation of the stoichiometry distribution we must reconstruct the spatial distribution from such a convolved image. This corresponds to a deconvolution of the raw data with the spectral distribution.

D. Formalism

To write the equations derived in paper T1 for convolution–deconvolution, we must in the remainder of this section distinguish between coordinates in the entrance plane (x_{in}) and in the exit plane (x_{out}). The entrance slit width of the spectrograph is spanned by coordinate x_{in}, and the y coordinate is parallel to the grooves of the grating. Including this 2-D extension and the factorization, the convolution [Eq. (8) of T1] for the specific case of 2-D Raman imaging reads as

$$T(x_{out}, y) = \int_{x_{in}} \eta(x', y) \times \left\{ \sum_i \sigma_i(x') \frac{g_i \exp[-(E_i/k_B T)]}{Z} \right\} \times N(x_{in}, y) I_L(x_{in}, y) \Delta t \, dx_{in}, \qquad (7)$$

in which $x' = [(x_{out} - x_{out,0}) - M_s(x_{in} - x_{in,0})]/\zeta$. Note that, although σ is a function of wavelength only, the spectrograph introduces an implicit dependence on x_{in} [Eq. (7) of paper T1]. To simplify this equation we can reintroduce the (single-species) spectral reference function [Eq. (11) of paper T1] as the result of a narrow-slit reference measurement in which a known number density $N_{ref}(y)$ is illuminated with laser intensity $I_{L,ref}(y)$ during Δt_{ref}, yielding

$$R(x', y) f_s = \eta(x', y) \times \left\{ \sum_i \sigma_i(x') \frac{g_i \exp[-(E_i/k_B T)]}{Z} \right\} \times N_{ref}(y) I_{L,ref}(y) \Delta t_{ref}, \qquad (8)$$

where f_s accounts for the fact that the infinitesimally narrow entrance slit has a finite width in practice, as discussed below. (The extent to which the temperature of the reference measurement may deviate from that of the actual imaging experiment depends on the sensitivity of the spectral contour to temperature, as discussed above.) For every individual species, therefore, one can write the corresponding Raman signal, by combining Eqs. (7) and (8), as

$$T(x_{out}, y) = \int_{x_{in}} \hat{R}[x_{out} - M_s(x_{in} - x_{in,0}), y] \times \left[\frac{\|R\|}{f_s} \frac{N(x_{in}, y)}{N_{ref}(y)} \frac{I_L(x_{in}, y)}{I_{L,ref}(y)} \frac{\Delta t}{\Delta t_{ref}} \right] dx_{in}. \qquad (9)$$

In Eq. (9) we split the measured spectral reference function into a normalized part ($\hat{R}$, the spectral profile), and its norm ($\|R\|$, the integrated intensity). If

raw data T are deconvolved with normalized part $\hat{R}$, the result (the whole term in the second set of brackets) will obviously be given in the same units as the measured data, T. On postnormalization of this result with $\|R\|I_L\Delta t/(f_s L_{L,\mathrm{ref}}\Delta t_{\mathrm{ref}})$, we express the desired number density distribution N in units of the reference distribution N_{ref}. Evidently, cross sections σ_i and the Boltzmann factor have disappeared from this formula. As previously for grating efficiency η and grating constant ζ, they have been incorporated into spectral reference distribution R. In this paper deconvolutions are performed with the normalized spectral reference function.

Factor f_s is a property of the specific OMA that is used in any OMA Raman imaging experiment. It depends on d_s, the width of the entrance slit. In a practical situation the image of the entrance slit is limited by the resolution of the CCD. The hypothetical infinitesimally narrow entrance slit of Eq. (9) of paper T1 is obtained experimentally for slit widths for which the image of the entrance slit no longer depends on d_s. This is the regime in which the image is below the resolution of the CCD, for which further decrease of d_s leads to a loss of intensity only. Therefore it is important for what d_s the spectral reference function is recorded. This dependence on d_s is accounted for explicitly by factor f_s. Note that $f_s(d_s)$ is the same for all species if their reference spectra are recorded at the same setting of d_s.

For a certain measurement $\mathbf{T} = \mathbf{t}$ the best reconstruction of the molecular distribution as it was imaged onto the entrance slit of the spectrograph is given by

$$N(x_{\mathrm{in}}, y) = \left\{ \frac{c(y)(\tau/\sigma)^2 - b\tilde{R}_{k=0}(y)}{\tilde{R}^2_{k=0}(y) + (\tau/\sigma)^2} + \mathrm{FT}^{-1}\left[\frac{\tilde{R}^*_{k,n_0}(y)\tilde{t}_k(y)}{|\tilde{R}_{k,n_0}(y)|^2 + (\tau/\sigma)^2} \right] \right\} g_{\mathrm{ref}}, \quad (10)$$

with

$$g_{\mathrm{ref}} = \frac{N_{\mathrm{ref}}(y) f_s}{\|\mathbf{R}(y)\|} \frac{I_{L,\mathrm{ref}}(y)}{I_L(x_{\mathrm{in}}, y)} \frac{\Delta t_{\mathrm{ref}}}{\Delta t},$$

according to the linear Bayesian deconvolution filter of Eq. (32) of paper T1. As in that paper, boldface symbols represent entire pixel rows of data. Equation (10) provides an algorithm with which to reconstruct $\mathbf{N}(y)$ in units of g_{ref}. If the reference molecular distribution is a uniform one, $\mathbf{N}_{\mathrm{ref}}(y)$ is equal for all rows.

Whether the deconvolved result is automatically corrected for laser sheet inhomogeneities depends on the experimental geometry. If the laser beam propagates parallel to the x_{in} coordinate (i.e., in the plane of spectral diffraction), the x_{in} dependency of the laser intensity, $I_L(x_{\mathrm{in}}, y)$, will disappear in the absence of attenuation. Consequently, laser intensity ratio $I_{L,\mathrm{ref}}(y)/I_L(x_{\mathrm{in}}, y)$ cancels any illumination inhomogeneity in the reconstructed image. If, however, the laser radiation propagates parallel to the grooves of the grating, that is, perpendicular to the dispersion coordinate, laser-sheet inhomogeneities express themselves as the dependence of I_L on x_{in}. In the experiments discussed in this paper the experimental configuration is such that the sheet of light propagates parallel to the grooves of the grating, and scattering and absorption losses in the medium are negligible. Because, however, reference spectra for methane could not be determined over the whole range of y, only one generic reference spectrum was used to deconvolve all pixel columns. Thus the deconvolved Raman images are not automatically corrected for laser-sheet inhomogeneities.

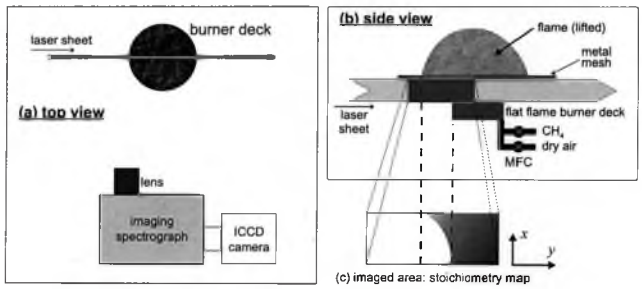

Fig. 4. Experimental setup; see text for details. (c) The rectangle shows an artist's impression of the expected stoichiometry distribution over the field of view of the detection system. The coordinate system used in the discussion is shown.

3. Experiment

The experimental setup is shown schematically in Fig. 4. A laminar flat flame burner developed at the University of Eindhoven[10] was used as the source of a premixed methane–air mixture. The flame was stabilized on a metal mesh at a distance of ~12 mm above the burner surface. Methane and dry air were obtained from gas bottles; the dry air was a 78.1:20.9 mixture of N_2 and O_2 [that is, $\beta = 3.73$ in Eq. (5)]. The stoichiometry could be adjusted by means of calibrated mass flow controllers (MFC; Bronkhorst Hi-Tec) in both gas supply leads.

The most appropriate illumination wavelength is a trade-off among Raman scattering cross section (which scales with λ^{-4}), detection efficiency (which depends on the detector), and, for this case, the separation of the Raman bands of the relevant chemical species. As the spectrograph available for these experiments could not sufficiently separate the spectral structure of N_2 from the (weak) $2\nu_4$ CH_4 line on 248-nm illumination, we used a tripled multimode Nd:YAG laser (Spectra-Physics QuantaRay 250-10: $\lambda \approx 355$ nm, 0.32-J/pulse, 5-ns pulse duration). Its circular beam was collimated by two positive cylindrical lenses into a sheet of approximately 10 mm × 0.1 mm [height × thickness (depth of field)]. Scattered light was detected perpendicular to the plane of the sheet of light and imaged by a camera lens (Nikon UV-Nikkor 105 mm, $f/4.5$) onto the entrance slit of an imaging spectrograph (ARC SpectraPro 300i, with a 2400-grooves/mm UV-blazed grating), as sketched at the left in Fig. 4.

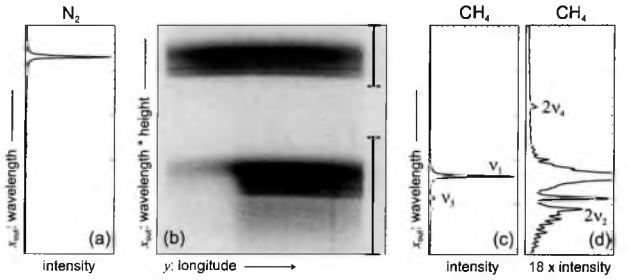

Fig. 5. Raw data Raman OMA graphs: (a) narrow slit measurement of ambient air; (b) broad slit measurement of a methane–dry-air flow at nominally stoichiometric conditions (for the field of view see Fig. 2); (c), (d) narrow slit measurements of a pure methane flow. All spectra are on different linear scales; image (b) is on a linear gray scale (white, low; black, high intensity).

The polarization of the incident laser light was rotated to be in the plane of the sheet of light to maximize the Raman-scattering efficiency. The spectrograph was oriented such that the grooves of its grating were parallel to the propagation vector of the laser sheet. It has an entrance slit of length $L_s = 30$ mm (Fig. 1) and a variable width (d_s along x_{in}, the dimension of diffraction) up to 3×10 mm. In the experiments the laser-sheet height (10 mm) was imaged to more-or-less match the maximum width of the entrance slit (upper right part of Fig. 4). The setup was found to be sensitive to the polarization of the scattered light,[11] and the detection efficiency could in principle be improved by use of a $\lambda/2$ plate in front of the imaging optics to optimize the polarization of the incident light. Because, however, a $\lambda/2$ plate with sufficiently large aperture was not available, we did not use this opportunity in the experiments reported here.

An intensified CCD (ICCD) camera (Fig. 4; Princeton Instruments ICCD-512T) collected the images at the exit port of the spectrograph. The OMA constructed in this way was aligned such that its field of view comprised both ambient air ($\Phi = 0$) and the premixed flow (Φ as set by the mass flow controllers); an artist's impression of the stoichiometry distribution that would be expected for this case is included in Fig. 4 (bottom right). With a narrow entrance slit (100 μm) the spectral resolution was approximately 0.033 nm/pixel (x_{out} dimension) and the spatial resolution amounted to 209 μm/pixel (in the y dimension) and, after deconvolution, 184 μm/pixel in the x dimension.

4. Results and Discussion

A. Average Stoichiometry

To test the performance of the deconvolution procedure we determined the stoichiometry distribution on the basis of an average over 25 accumulations of 250 laser pulses each (well over 10-min measurement time in total). The raw data, taken for a stoichiometric methane–air mixture, are shown in Fig. 5(b); the coordinate system used is indicated in Fig. 4. As introduced in Eq. (1), an asterisk refers to the convolution of spatial and spectral information and $x = x_{out}$ denotes the spatial axis at the exit port of the spectrograph. Two bands are distinguished in the raw data of Fig. 5(b); the upper one is due to N_2 (present in the flow as well as in ambient air) and the lower one is due to CH_4 (present only in the flow). Both bands are truncated at the right (the N_2 band also at the left) by finite entrance slit length L_s of the spectrograph; the slit width was set to $d_s = 3.10$ mm. The signal-to-noise ratio (S/N) can be defined as the ratio of the average pixel value (in a certain region) to the standard deviation (1σ), assuming uniform gas density and illumination intensity. It was determined for the two bands over a probe area of 100×20 pixels located within the main flow, resulting in a S/N of 11 in the N_2 band and a S/N of 12 in the CH_4 band. Part of the structure along the x_{out} direction is due to laser-sheet inhomogeneity. This shows up in both the N_2 and the CH_4 bands but will cancel in the calculation of Φ [Eq. (5)] because of the linear dependency of the Raman signal on laser power density I_L (Section 2). Besides this, the CH_4 band shows a distinct wing extending to the red [bottom of the OMA graph in Fig. 5(b)], which is due to the structure of the Raman spectrum (Fig. 2).

Both the N_2 and the CH_4 images need to be deconvolved with a proper spectral reference function, as discussed at the end of Section 2. To this end, narrow-slit spectra ($d_s = 0.10$ mm) were taken for ambient air and for a pure methane flow [Figs. 5(a), 25×71 laser pulses, and 5(c) and 5(d), 25×5 laser pulses, respectively] for the same setting of the grating, that is, equivalent x_{out} axes. As only the right-hand part of the imaged region was covered with a flow out of the burner, it was not possible to record a CH_4 spectrum for every longitude. Therefore the reference spectra $\mathbf{R}^{N_2} f_s$ ($d_s = 0.10$ mm) [Fig. 5(a)] and $\mathbf{R}^{CH_4} f_s$ ($d_s = 0.10$ mm) [Fig. 5(c)] are averages over a narrow range in the flow. These spectra serve as the (nonnormalized) species-specific spectral reference functions for deconvolution of the OMA graph in Fig. 5(b). If the species-specific parts of this figure, indicated by the I-bars in Fig. 5(b), are isolated and deconvolved with their corresponding spectral reference functions, the reconstruction shown in Fig. 6(c) results. This image shows the best reconstructions of the individual N_2 and CH_4 intensity distributions obtained with recentered, normalized spectral reference functions. Therefore the reconstructed data remain in the position of the raw data (for N_2 as well as for CH_4). Because the reconstructions were not postnormalized for reference conditions, the gray scale is the same intensity scale as that for the raw data [see the discussion below Eq. (9)]. Note that structure that is due to the $2\nu_4$ CH_4 band (between the N_2 and the main CH_4 images) is discarded by judicious choice of the processed regions (I-bars) in Fig. 5(b).

In comparison to the raw data [depicted also in Fig. 6(a) for comparison], in the reconstructed data the contrast in both bands has increased. The boundaries have become sharper (as they should, because they are determined by the entrance slit), and the

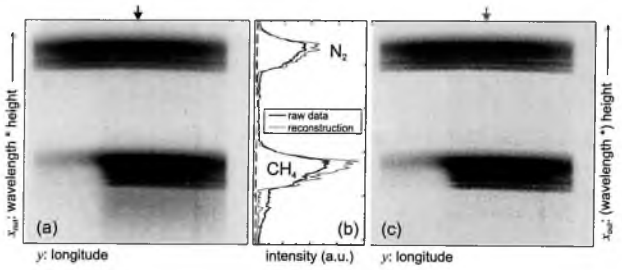

Fig. 6. (a) Raw data and (c) deconvolved Raman OMA graphs of a methane–dry-air flow at nominally stoichiometric conditions (for the field of view see Fig. 3). Both images contain a N_2 (top) and a methane (bottom) contribution, which are truncated at the left and the right by the spectrograph entrance slit length. The vertical axis of (c) contains the label (wavelength $*$), as it is purely spatial only within the N_2 and CH_4 reconstructions (see text for computational details). Vertical cross sections through the images of (a) (raw data) and (c) (reconstruction) at the locations indicated by the arrows are plotted in (b). All images are on the same linear intensity scale.

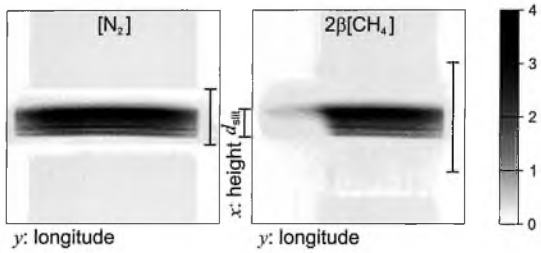

Fig. 7. Results of deconvolution of the raw data [Fig. 4(b)] according to Eq. (10) with $\mathbf{R}^{N_2}$ [Fig. 4(a)] for $[N_2]$ and with $\mathbf{R}^{CH_4}$ [Fig. 4(c)] for $[CH_4]$. The latter was postmultiplied by 2β. Both images are (i) on a purely spatial scale in both dimensions; (ii) on the same gray scale; and (iii) in units of $[N_2]_{amb} I_{L,ref}(y) f_s(d_s = 0.10\ \text{mm})/I_L(y)$, that is, still dependent on the laser-sheet inhomogeneity. For clarity the error bars indicate the parts that were selected in Fig. 4(b) for species-specific deconvolution as well as the actual width of the entrance slit.

spectral tail below (to the red of) the CH_4 band has all but disappeared, as can be seen more clearly from Fig. 6(b), which shows a vertical cross section that is one pixel wide through Fig. 6(c) [location of the lighter arrow at the top of Fig. 6(c) and lighter curve in Fig. 6(b)]. For comparison, the corresponding cross section through the raw data of Fig. 6(a) is included as well [darker curve in Fig. 6(b)]. The structure along the x_{in} direction that remains in the deconvolved N_2 image is due largely to intensity variations in the laser-light sheet. The CH_4 band shows the same variation (one of the advantages of using a spectrograph: both bands are really measured simultaneously), but in addition there is some residual structure that is due to incompletely removed spectral features of CH_4, similar to the ghost images in Fig. 6(b) of paper T1.

Postnormalization of the deconvolution result automatically takes into account the different Raman scattering cross sections of N_2 and CH_4. Consequently, the pixel values in Fig. 6(c) can be considered relative partial number densities with respect to $N_{ref}^{s}(y)$. A minor complication arises from the fact that the reference spectral distributions for N_2 were measured for dry air rather than for pure N_2. Most conveniently, all number densities in the various flows can be expressed in terms of the number density of N_2 in dry ambient air, $[N_2]_{amb}$. The flow, with an exit speed of the order of 24 cm/s, is treated as incompressible; that is,

$$[O_2]_\Phi + [N_2]_\Phi + [CH_4]_\Phi = [O_2]_{amb} + [N_2]_{amb} = \frac{\beta + 1}{\beta}[N_2]_{amb}, \quad (11)$$

for any composition of the methane–dry-air mixture, including the limiting cases of pure methane ($\Phi \to \infty$) and dry air ($\Phi = 0$). For a premixed flow of stoichiometry Φ, the N_2, O_2, and CH_4 concentrations read as

$$[N_2]_\Phi = \frac{2(\beta + 1)}{2 + 2\beta + \Phi}[N_2]_{amb}, \quad (12a)$$

$$[O_2]_\Phi = \frac{2(\beta + 1)}{\beta(2 + 2\beta + \Phi)}[N_2]_{amb}, \quad (12b)$$

$$[CH_4]_\Phi = \frac{(\beta + 1)\Phi}{\beta(2 + 2\beta + \Phi)}[N_2]_{amb}. \quad (12c)$$

In particular, the reference concentrations for the spectral reference function read as

$$[CH_4]_{ref} = \frac{\beta + 1}{\beta}[N_2]_{amb}, \qquad [N_2]_{ref} = [N_2]_{amb} \quad (13)$$

for pure methane and for ambient air, respectively. After normalization to this ambient nitrogen concentration and correction for the number of laser pulses, the $[N_2]$ and $2\beta[CH_4]$ (with $\beta = 3.73$) images are as shown in Fig. 7 (the deconvolution is performed with the normalized spectral reference functions at their original positions, i.e., not recentered). Both now purely spatial patterns are centered vertically in the images: The deconvolution automatically ensures the correct spatial alignment (a property of Fourier transforms). Furthermore, both images are on the same gray scale in units of $\{[N_2]_{amb} f_s(d_s = 0.10\ \text{mm}) I_{L,ref}(y)/I_L(y)\}$. This unit cancels on a pixel-by-pixel division of the two images, resulting in the dimensionless 2-D stoichiometry distribution, according to Eq. (5).

Figure 8 shows stoichiometry distributions derived from 625 single-shot accumulations at various preset mixing ratios. At the left the experimental conditions are indicated [set value for Φ; number of laser shots (#) for the raw data acquisition], and at the right the spatially averaged stoichiometry as determined from the images is listed [average and one standard deviation over a rectangular region of 10^4 pixels in the central part of the flow, indicated by the

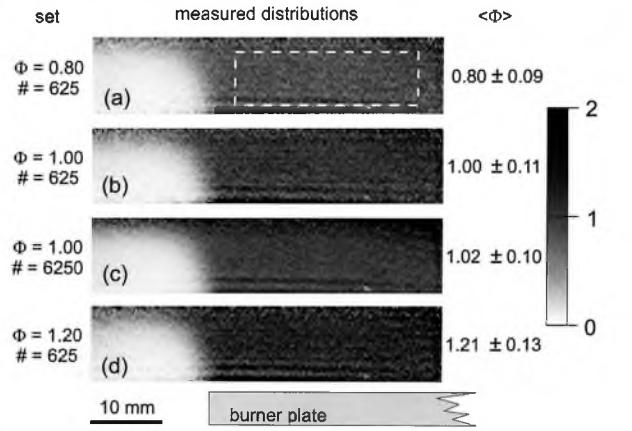

Fig. 8. Average stoichiometry distributions, derived from images like those of Fig. 6. Experimental settings are indicated at the left; the spatially averaged stoichiometries derived from the images are listed at the right [region involved indicated in (a)]. All deconvolutions were performed for $\sigma/\tau = 6$ counts^{-1}.

dashed rectangle in Fig. 8(a)]. Clearly, the averages reproduce the nominal values very well, with about 10% statistical error. Part of the error is due to the residual (spectral) structure in the images, as discussed above (the horizontal streak pattern in the images). For this reason, increasing the data collection time by a factor of 10 [cf. Figs. 8(b) and 8(c)] does not improve the S/N by a factor of $\sqrt{10}$, as would be expected for shot-noise-limited data. Note also that the fanning out of the flow near the upper limit of the field of view, where the flow bumps into the metal mesh, can clearly be seen. (The corresponding feature at the right-hand side of the flow falls outside the field of view; see Fig. 4.)

B. Snapshot Stoichiometry

The full advantage of imaging through a spectrograph would be exploited if signal levels were high enough to permit accurate stoichiometry determinations with single laser shots. An example of such a single-shot acquisition is shown in Fig. 9 for nominally stoichiometric conditions ($[N_2]_{\Phi=1} = 0.90[N_2]_{amb}$ and $[CH_4]_{\Phi=1} = 0.12[N_2]_{amb}$). Although the S/N of Fig. 9 may be less than what is achievable with 2-D optical bandpass filtering, the merit of 2-D OMA imaging is

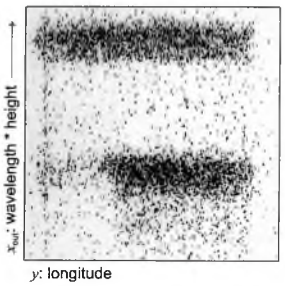

Fig. 9. Single-shot Raman image from a flow in nominally stoichiometric conditions. Linear, inverted gray scale from $0 \leq I$ [counts] ≤ 150.

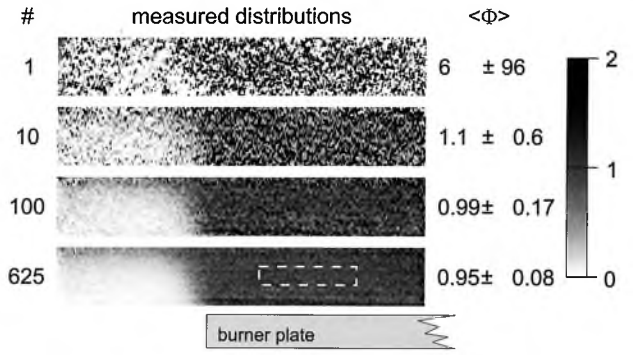

Fig. 10. Stoichiometry distributions determined from different numbers of laser shots. Spatial averages and standard deviations are determined in the dashed rectangular region (4050 pixels) of the stoichiometry for 625 laser pulses. See text for discussion.

that all species are imaged simultaneously for exactly the same spatial region.

For the current experimental setup (illumination intensity as much as 60 MW/cm^2), we have determined the statistics of stoichiometry distributions for averages over a number of single-shot images such as Fig. 9. After this averaging, the deconvolution algorithm was applied as discussed in Subsection 4.A, followed by division of the CH_4 image by the N_2 image. Each of the stoichiometry images presented below is in fact the worst-case average over a number of laser shots (owing to the CCD read-out noise) recorded on a nominally stoichiometric ($\Phi = 1$) flow. Part of the results are shown in Fig. 10, which shows the distributions and the S/N values that result from averages over 1, 10, 100, and 625 single-shot images. In the present setup, obtaining a stoichiometry distribution with a spatially averaged S/N of $\approx$1 requires fewer than 10 laser shots. This performance increases a S/N of 10 when more than 250 laser shots are used. In the single-shot image the regions with and without flow are recognizable, but the statistics are very poor and do not allow one to estimate stoichiometry values accurately.

There is, however, room for improvement now that the major obstacle (the deconvolution procedure) has been tackled. One can increase the count rate by increasing the laser fluence and by increasing the detection efficiency. Obviously, the laser pulse energy could be increased but such an increase would be limited by the occurrence of optical breakdown. Also, the laser could be multipassed through the probe volume.[12,13] On the detection side, the efficiency is limited by the collection angle of the spectrograph ($f/4$ for the ARCSpectraPro 300i). Improvement could be achieved by binning pixels on the CCD chip, at the expense of spatial resolution. Optimization of the setup with respect to the polarization of the scattered light promises a potential gain of at most a factor of 2.5.[11] Finally, there are prospects (currently under study) to improve the deconvolution procedure further, to reduce the residual (ghost) structure.

5. Conclusions

Raman imaging through a grating spectrograph is useful for determination of two-dimensional stoichiometry distributions. The main advantage of the method is the really simultaneous determination of fuel and oxidizer distributions over exactly the same field of view and under exactly the same experimental conditions. Moreover, the spectrograph is a permanent monitor of the spectral purity of the data. The raw data, which consist of a convolution of the spectral and spatial intensity distributions in the spectrograph entrance plane, can be quantified as separate, purely spatial distributions of both fuel and oxidizer through the application of a dedicated Bayesian deconvolution filter. These patterns directly yield the stoichiometry field. The signal-to-noise ratio is limited because of the low Raman scattering cross sections. Spatial averages of the stoichiometry in uniform parts of a methane–air flow reproduce the set values with a statistical error below 10% when 250 or more single-shot images are averaged.

We appreciate the stimulating discussion of this subject with Michael Golombok. This research was made possible by financial support from the Technology Foundation, the Applied Science Division of the Netherlands Organisation for Scientific Research, and the technology program of the Ministry of Economic Affairs.

References

1. R. A. L. Tolboom, N. J. Dam, J. J. ter Meulen, J. M. Mooij, and J. D. M. Maassen, "Quantitative imaging through a spectrograph. 1. Principles and theory," Appl. Opt. **43,** 5669–5681 (2004).
2. R. A. L. Tolboom, N. J. Dam, N. M. Sijtsema, and J. J. ter Meulen, "Quantitative spectrally resolved imaging through a spectrograph," Opt. Lett. **28,** 2046–2048 (2003).
3. I. Glassman, *Combustion*, 3rd ed. (Academic Press, San Diego, Calif., 1996).
4. J. Warnatz, U. Maas, and R. W. Dibble, *Combustion* (Springer-Verlag, Berlin, 1996).
5. A. C. Eckbreth, *Laser Diagnostics for Combustion Temperature and Species*, Vol. 7 of Energy and Engineering Science Series, A. K. Gupta and D. G. Lilley, eds. (Abacus, Cambridge, Mass., 1988).
6. K. Kohse-Höinghaus and J. B. Jeffries, eds., *Applied Combustion Diagnostics* (Academic, San Diego, Calif., 2002).
7. R. B. Miles, "Flow-field diagnostics," in *Applied Combustion Diagnostics*, K. Kohse-Höinghaus and J. B. Jeffries, eds. (Academic, San Diego, Calif., 2002), pp. 194–223.
8. G. Herzberg, *Infrared and Raman Spectra of Polyatomic Molecules*, Vol. II of Molecular Spectra and Molecular Structure (Van Nostrand Reinhold, New York, 1945).
9. H. W. Schrötter and H. W. Klöckner, "Raman scattering cross sections in gases and liquids," in *Raman Spectroscopy of Gases and Liquids*, A. Weber, ed., Vol. 11 of Topics in Current Physics (Springer-Verlag, Heidelberg, Germany, 1979), pp. 123–166.
10. A. van Maaren, D. S. Thung, and L. P. H. de Goey, "Measurement of flame temperature and adiabatic burning velocity of methane/air mixtures," Combust. Sci. Technol. **96,** 327–344 (1994).
11. R. Tolboom, "Expanding laser diagnostics in non-seeded compressible flow research," Ph.D. dissertation (University of Nijmegen, Nijmegen, The Netherlands, 2002), available from http://webdoc.ubn.kun.nl/mono/t/tolboom_r/expaladii.pdf.
12. M. B. Long, P. S. Levin, and D. C. Fourguette, "Simultaneous two-dimensional mapping of species concentration and temperature in turbulent flames," Opt. Lett. **10,** 267–269 (1985).
13. R. W. Schefer, M. Namazian, and J. Kelly, "Simultaneous Raman scattering and laser-induced-fluorescence for multispecies imaging in turbulent flames," Opt. Lett. **16,** 858–860 (1991).